ACS OMEGA

Open Access

http://pubs.acs.org/journal/acsodf

Article

First-Principles Study of Penta-PtXY (X = Se, Te; Y = S, Te; X ≠ Y) Monolayer with Highly Anisotropic Electronic and Optical Properties

Ting Yang, Cuixia Yan,* Shi Qiu, Yanghao Tang, Ao Du, and Jinming Cai*

Cite This: *ACS Omega* 2024, 9, 32502−32512

Read Online

ACCESS | Metrics & More | Article Recommendations | Supporting Information

ABSTRACT: Two-dimensional (2D) semiconducting materials with anisotropic physical properties have induced lively interest due to their application in the field of polarizing devices. Herein, we have designed a family of penta-PtXY (X = Se, Te; Y = S, Te; X ≠ Y) monolayers and predicted the electronic and optical properties based on the first-principles calculation. The results suggest that the penta-PtXY (X = Se, Te; Y = S, Te; X ≠ Y) monolayers are indirect-gap semiconductors with a medium bandgap of 2.29−2.66 eV. The penta-PtXY (X = Se, Te; Y = S, Te; X ≠ Y) monolayers own a remarkable mechanical anisotropy with a high Young's modulus anisotropic ratio (3.0). In addition, the penta-PtXY (X = Se, Te; Y = S, Te; X ≠ Y) monolayers exhibit a high anisotropy ratio of hole/electron mobility in the *x* and *y* directions (1.16−3.54). The results calculated by the G_0W_0+BSE method indicate that the single-layers also bear a salient optical anisotropy ratio (1.56−2.11). The integration of the anisotropic electronic, optical, and mechanical properties entitles penta-PtXY (X = Se, Te; Y = S, Te; X ≠ Y) monolayers as potential candidates in multifunctional polarized nanodevices.

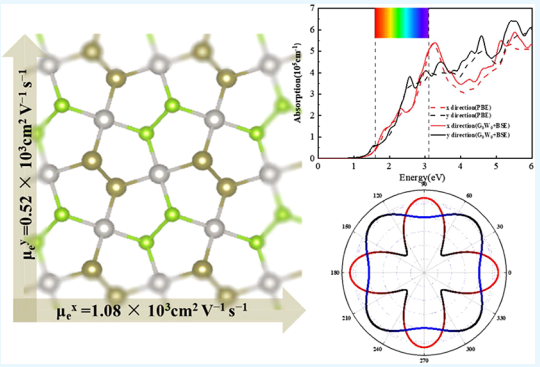

INTRODUCTION

In-plane anisotropic two-dimensional materials (referred to as anisotropic 2D materials in the work) have unique electronic and optical anisotropy due to their anisotropic energy band structure and their rich atomic arrangement. It provides them with additional freedom in device design, making them promising for a broad scale of applications in the field of polarization-sensitive nanodevices, especially polarization-sensitive photodetectors based on anisotropic 2D materials. They offer meaningful advantages over conventional thin-film photodetectors with respect to both high sensitivity and remote detection, which makes them rapidly becoming an attractive nanomaterial and one of the current research hotspots.

In the last several years, many anisotropic 2D materials[1−9] have been obtained, such as single black phosphorus (BP),[10] GaTe,[11] and ReQ_2 (Q = S, Se).[12,13] However, most of the anisotropic 2D materials studied have some deficiencies in practical applications, such as poor stability of BP,[10] GeP,[3] and GaTe,[11] low anisotropy ratios of ReQ_2,[12,13] GeSe,[4] and Ta_2NiS_5[6] and low current switching ratios of $TaIrTe_4$.[7] Despite the variety of anisotropic 2D materials that have been discovered, few 2D materials possess practical characteristics such as high stability and a large in-plane anisotropy ratio, which hinders the development of anisotropic 2D materials in the field of polarization nanodevices. Therefore, it is important to explore anisotropic 2D materials with these practical characteristics. It is well-known that the low symmetry and folded structure can provide favorable conditions for the anisotropy of materials. A BP monolayer with a folded structure exhibits significant in-plane anisotropy.[10] Also, the 2D materials MNX and Be_2C with unique fold structures have also been predicted to own anisotropy.[14,15] 2D materials derived from the Cairo pentagonal topology structure (referred to as pentagons) have low structural symmetry compared to the traditional 2D materials with predominantly a hexagonal or quadrilateral structure, which provides a new idea for searching for anisotropic 2D materials. Importantly, the pentagonal 2D structure overcomes the "isolated pentagonal rule"[16,17] and can exist stably due to the fold structure, which is another favorable condition for presenting anisotropy. Thus, the pentagonal 2D structure, combining both low symmetry and high foldability, is easy to exhibit anisotropy. Gu et al. have synthesized a pentagonal 2D $PdSe_2$ structure experimentally, which has a high in-plane anisotropy of optical and electronic properties as well as a high stability.[18] PdPSe is another pentagonal 2D material obtained experimentally.[16] It has high stability, superior optical and electronic anisotropy, a high photo-

Received: January 24, 2024
Revised: April 25, 2024
Accepted: June 18, 2024
Published: July 18, 2024

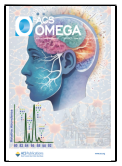

detection and conductivity anisotropy ratio of 6.17 and 3.85, respectively, and a current switching ratio of 10^8, which is better than most anisotropic 2D materials. The pentagonal 2D structure of PdPS has been obtained by the mechanical exfoliation method, which has a superior anisotropy.[19] The carrier mobility and photocurrent anisotropy ratios reach 3.9 and 2.3, respectively, with a current switching ratio of about 10^8 and a photoresponsivity of 5.2×10^4 AW^{-1}. The first-principles calculation results have shown that the pentagonal 2D BCN and BNSi structures are highly stable and have significant optical anisotropy in the UV and visible regions with ultrahigh hole mobility and anisotropy ratios.[20,21] In addition, other pentagonal 2D structures are predicted to be stable by calculations, such as NiX_2 (X = S, Se, Te),[22] RhS_2,[23] CNP,[24] and PBN.[25] However, their anisotropy in electronic and optical properties has not been reported.

These excellent, comprehensive properties suggest that all of the abovementioned pentagonal 2D materials possess characteristics of practical value, such as high stability and a high anisotropy ratio. However, only a few materials have been studied so far. Moreover, the intrinsic correlation between the pentagonal 2D structure and the anisotropy of electronic and optical properties urgently needs to be explored to discover more such materials for the development of polarized nanodevices. The compounds containing the elements of group VIII B and VI A group excess $PdSe_2$,[26−28] PdX_2 (X = S, Se, Te),[29] have not been studied for their anisotropy of electronic and optical properties yet.

In this work, on the basis of previous studies,[30−33] considering their semiconductor properties, we have studied the sixth main group of nonmetallic elements S, Se, and Te and have designed a penta-PtXY (X = Se, Te; Y = S, Te; X ≠ Y) monolayer structure. Based on density functional theory (DFT), the optical and electronic properties of anisotropy were investigated. The consequences indicate that the penta-PtXY (X = Se, Te; Y = S, Te; X ≠ Y) monolayers possess high dynamic, thermal, and mechanical stability, which have been demonstrated by the phonon spectroscopy and ab initio molecular dynamics (AIMD) results. The electronic and optical properties of the stable framework in the *x* and *y* directions have been investigated. The penta-PtXY (X = Se, Te; Y = S, Te; X ≠ Y) structures are indirect semiconductors with band gaps of 2.29−2.66 eV, and their light absorption coefficients are up to 10^5 cm^{-1} both in the *x* and *y* directions. Also, penta-PtSeTe hole carrier mobility in the *y* direction reaches 518.06 cm^2 $V^{-1}s^{-1}$. The work provides a theoretical basis for for experimental synthesis. In addition, these properties are crucial for the development of new materials and the design of new electronic devices, making the design of tunable electronic devices promising for a wider range of applications. In addition, this anisotropic material can also be applied in electromagnetic shielding and optical devices to meet the specific needs of different directions.

COMPUTATIONAL METHODS

First-principles calculations were conducted employing the Vienna ab initio simulation package,[34,35] with a settled plane-wave dynamics cutoff energy set at 500 eV. The electronic exchange-correlation energy was treated within the Perdew−Burke−Ernzerhof (PBE) functional under the framework of the generalized gradient approximation (GGA).[36] Moreover, the HSE06 hybrid functional[37] was chosen for more accurate computation of electronic band structures. The valence electrons being considered are 4s and 4p electrons of the Se atom; 3s and 3p electrons of the S atom; 5s and 5p electrons of the Te atom; and 5d and 6s electrons of the Pt atom. The nuclear electrons were processed by projector-augmented-wave pseudopotentials.[38,39] The geometry optimization was carried out until the Hellmann−Feynman force aiming at each atom was not more than 0.01 eV/Å in every direction. Initially, a 10 × 10 × 1 Monkhorst−Pack *k*-grid was employed for Brillouin zone sampling during geometry optimization, later expanded to 25 × 25 × 1 for static total energy calculations.[40] To minimize artificial interactions between adjacent layers, a 20 Å vacuum layer along the *z*-axis was pulled. Also, in all self-consistent runs, the convergence criterion was set to 10^{-7} eV for total energy. Phonon dispersion analysis was conducted employing density functional perturbation theory (DFPT) through the PHONOPY code.[41] The PBE functions and the NVT canonical ensemble were utilized by AIMD simulations to assess the thermal stability. In addition, the simulation involved a 3 × 3 × 1 supercell at elevated temperatures (1200 or 1300 K) with each emulation lasting 10 ps and employing a time step of 1 fs.

RESULTS AND DISCUSSIONS

Geometric Structure and Stability. The optimized structures of penta-PtXY (X = Se, Te; Y = S, Te; X ≠ Y) single-layers are shown in Figure 1.The penta-PtXY (X = Se, Te; Y = S, Te; X ≠ Y) is abbreviated as the penta-PtXY hereafter. The top view (as seen in Figure 1a) shows that the penta-PtXY structure is composed entirely of pentagons, forming a beautiful pattern similar to the geometry of penta-graphene.[42] The unit cell is marked by a dashed line, which contains 6 atoms (2 Pt, 2 X, and 2 Y atoms). The Pt atoms in the single-cell are combined with two opposing X atoms (X = Se, Ti) and Y atoms (Y = Se, Ti) to form a curved tetracoordinate configuration. It is worth mentioning that the unit cell is centrosymmetric. From the side views in Figure 1b, the buckling is observed, which leads to a fold structure for penta-PtXY.

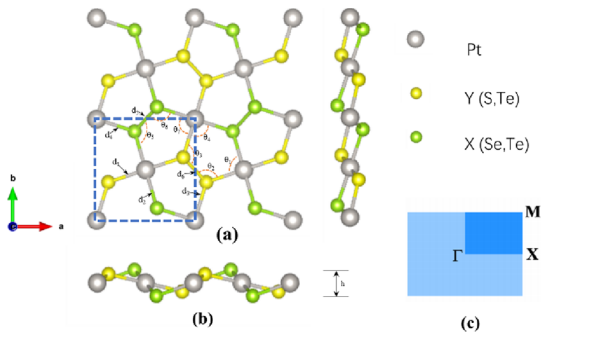

Figure 1. (a) Top view and (b) side view of the penta-PtXY monolayer, with the unit cell delineated by a dashed-line rectangle. (c) 2D Brillouin zone of penta-PtXY monolayer, featuring high-symmetry k-points.

The optimized lattice constants are shown in Table 1. It can be found that the bond lengths of penta-PtSeS and penta-PtSeTe are similar to the ones of the previous studies on PtSSe[43] and PtSeTe.[44] The bond lengths of penta-PtXY increases with the atomic number, which is consistent with the bond length rule in PdPX (X = O, S, Te).[45]

https://doi.org/10.1021/acsomega.4c00803
ACS Omega 2024, 9, 32502−32512

Table 1. Lattice Constants a and b, Bond Lengths, Bond Angles θ_{1-7}, Thicknesses h, Cohesive Energies per Atom E_{coh}, Thicknesses h, of Penta-PtXY

system	a, b (Å)	d_{1-6} (Å)	θ_{1-7} (deg)	E_{coh} (eV/atom)	h	PBE (eV)	HSE06 (eV)
penta-PtSeS	5.57 5.70	2.34 2.43 2.33 2.44 2.43 2.18	87.21 102.57 107.18 94.41 97.39 93.32 85.59	4.68	1.67	1.47	2.66
penta-PtTeS	5.65 5.84	2.36 2.58 2.36 2.60 2.79 2.20	88.21 103.21 109.7 95.73 89.12 84.06 84.27	4.48	2.21	1.44	2.35
penta-PtSeTe	5.8 6.12	2.61 2.45 2.59 2.48 2.49 2.79	85.12 89.16 95.43 92.64 106.32 99.18 87.36	4.32	1.98	1.49	2.29

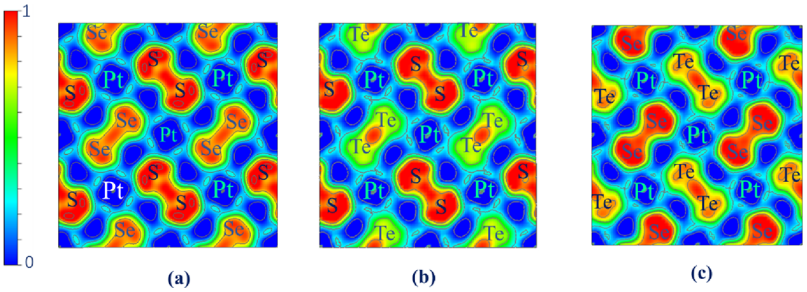

Figure 2. Electron localization functions of (a) penta-PtSeS, (b) penta-PtTeS, and (c) penta-PtSeTe. The calculations were performed using 2 × 2 supercells and the PBE functional.

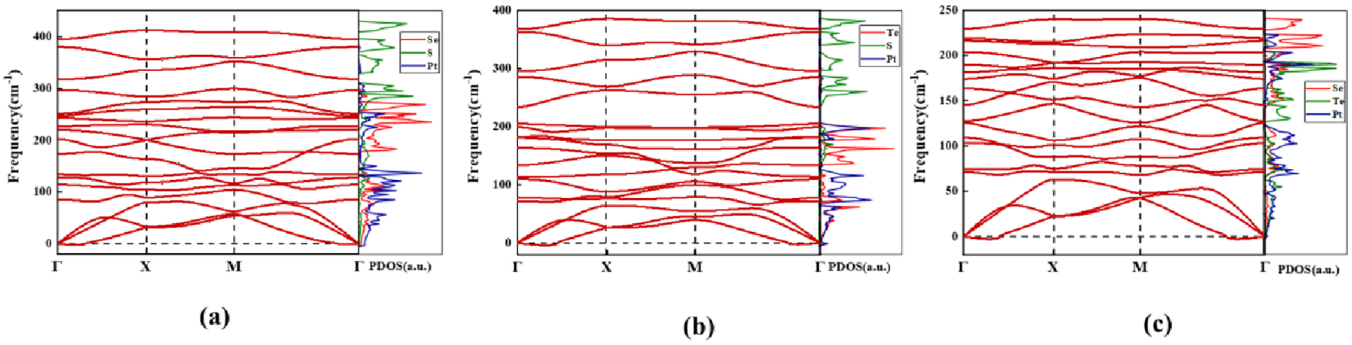

Figure 3. Phonon spectra and phonon density of states of (a) penta-PtSeS, (b) penta-PtTeS, and (c) penta-PtSeTe.

In practical applications, the 2D penta-PtXY structure may react with gas molecules in the environment to destroy the structure of the material. Therefore, we explored the possible interaction between the 2D penta-PtXY structure and oxygen molecules. We mainly studied the adsorption behavior of O_2 on 2D penta-PtXY structures. Here, the adsorption energy E_{ads} is defined as $E_{ads} = E_{tot} - E_{host} - E_{o_2}$,[46] where E_{tot} represents penta-PtXY structure energy, E_{host} represents the energy of the penta-PtXY structure without adsorption of external molecules, and E_{o_2} is defined as the energy of oxygen molecules. Figure S1 shows the possible adsorption configurations of O_2 on the surfaces of penta-PtSeS monolayers, penta-PtTeS, and penta-PtSeTe. Here, for the oxygen molecule, we consider eight adsorption configurations including hollow, Pt atom top, X atom top, Y atom top, Pt-X bond bridge, and Pt−Y bond bridge, X−X bond bridge, and Y−Y bond bridge. Through calculation, we find that their adsorption energy is small. The most stable adsorption configuration is indicated by the black box in Figure S1. The adsorption energy of O_2 on the surface of penta-PtSeS monolayers, penta-PtTeS, and penta-PtSeTe is as follows: −0.034, −0.134, and −0.03 eV, respectively. Moreover, the distance between the ambient gas molecules and the penta-PtXY monolayer is in a wide range (3.02−3.54 Å), indicating that there is a weak van der Waals interaction between them. The adsorption of the O_2 molecule does not affect the penta-PtXY structural stability.

To investigate the bonding characteristics of the monolayer penta-PtXY, the electron localization function (ELF) has been calculated (as shown in Figure 2), which can describe the localization among X atoms, Y atoms, and Pt atoms. Commonly, the ELF measures of 0.99, 0.50, and 0.00 imply a fully localized electron state, a fully nonlocalized electron state, and a very low charge density state. The electrons near Pt positions (blue regions) are deficient, and the electrons are located near the X and Y atoms. This means that the X and Y atoms accept the electrons from the Pt atoms. The iconic bond is formed between the Pt atom and X and Y atoms. For the bonding between X and Y atoms, the covalent bonds are obviously observed, which are due to the hybridization of the X and Y atomic orbitals. A small electron density appears in the gap regions (light regions). It is considered that the electrons of the X and Y atoms are provided by the Pt atom. The formation of those bonds helps to improve the stability of the penta-PtXY structure. It is noted that the electron density around the Te−Te bond (in Figure 2b) is obviously lower than that of the Se−Se bond (in Figure 2a). It is considered that the electronegativity of the Te atom is smaller compared to that of the Se atom, which leads to the Te atom accepting a lower electron. Due to a similar reason, compared with Figure 2a, the charge density at the Se atom in Figure 2c is higher, while the charge density around the Te atom is significantly lower.

To identify the energy stability of penta-PtXY, we have reckoned their cohesive energies that are determined as E_{coh} =

https://doi.org/10.1021/acsomega.4c00803
ACS Omega 2024, 9, 32502−32512

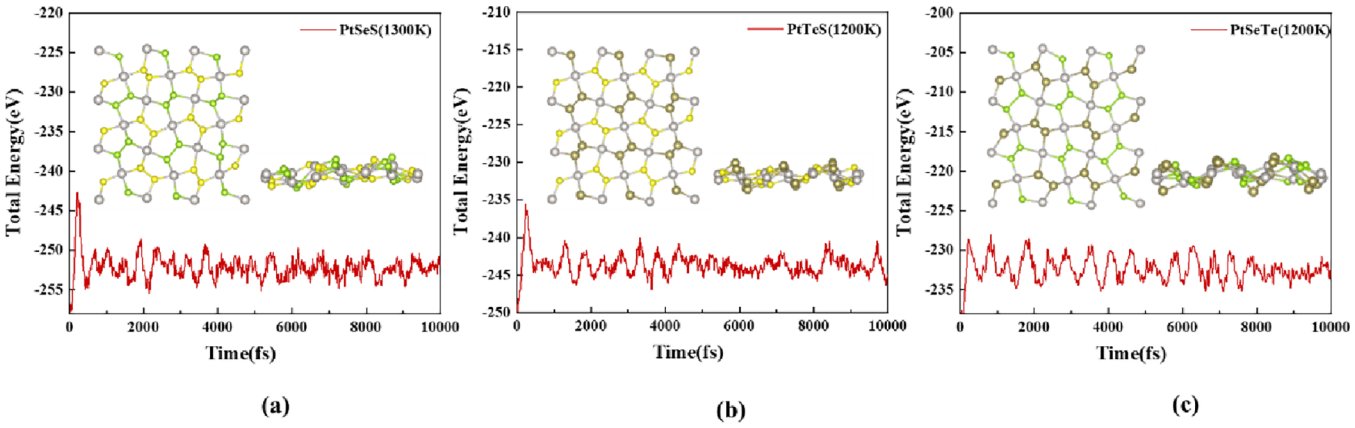

Figure 4. Total potential energy fluctuation during AIMD simulation at: (a) 1300K (penta-PtSeS), (b) 1200 K (penta-PtTeS), and (c) 1200 K (penta-PtSeTe) (3 × 3 × 1 supercell for the three structures).

Table 2. Calculated Elastic Constants C_{ij}, Young's Modulus E of the Penta-PtXY Single Molecular Layer, and Poisson's Ratio ν

structure	C_{11}	C_{22}	C_{12}	C_{66}	E	ν
penta-PtSeS	60.59	60.59	16.28	27.31	56.21	0.27
penta-PtTeS	44.67	44.67	14.12	23.79	40.21	0.37
penta-PtSeTe	36.52	64.26	1.60	23.07	36.48(x) 64.19(y)	0.03(x) 0.04(y)
graphene[55]	352.7	352.7	60.9	145.9	342.2	0.173
BN[56]	289.8	289.8	63.7	113.1	275.8	0.220
penta-graphene[57]	265	65	−18		263.8	−0.068

$(2E_{Pt} + 2E_X + 2E_Y - E_{tot})/6$ where E_{Pt}, E_X, E_Y, and E_{tot} are the energy of isolated Pt atoms, isolated X atoms, and isolated Y atoms, and the energy of penta-PtXY monolayer, respectively. From Table1, it is found that the cohesive energy is 4.68/4.48/4.32 eV/atom for penta-PtSeS/PtTeS/PtSeTe and is positive, which indicates that the structure of penta-PtXY is energetically favorable. In comparison, the cohesive energies of penta-PtXY exceed those of phosphorene (3.44 eV/atom)[47] and silicone (3.94 eV/atom).[48] While they are lower than that of graphene (7.97 eV/atom),[49] penta-PtXY exhibits superior stability compared to phosphorene and silicene, both of which have been effectively composed experimentally. Notably, the cohesive energy of penta-PtSeTe is less than that of penta-PtSeS and penta-PtTeS.

To explore the kinetic stability of penta-PtXY, phonon dispersion calculations have been conducted. The phonon spectra and projected phonon state densities of penta-PtXY are given in Figure 3. For the three structures, they all have tiny imaginary frequencies (less than −5 cm^{-1}) at the Γ point (as seen in Figure 3a−c). The imaginary frequency can be eliminated by expanding the cell.[50] Penta-PtTeS monolayer is selected randomly and expanded to 5 × 5 × 1. It is found that the virtual frequency is disappear (in Figure S2). It implies that the three structures are stable dynamically.[50] Furthermore, it is worth mentioning that the highest frequency is 412 cm^{-1} for penta-PtSeS, which is comparable to the frequencies of MoS_2 (473 cm^{-1}),[51] phosphorene(440 cm^{-1}),[52] and PdPTe (460 cm^{-1}).[45] For penta-PtSeS and penta-PtTeS single-layers, as the phonon density of states results show, the two highest optical modes come from the contribution of S atoms. Also, the projected phonon state densities indicate that the penta-PtXY bonds are fairly robust.[53]

Next, the thermal stabilities of the penta-PtXY monolayers were inspected by AIMD simulations. Figure 4 shows the variation of free energy and atomic configurations of penta-PtXY monolayers at high temperatures, which are 1300 K for penta-PtSeS, 1200 K for penta-PtTeS, and 1200 K for penta-PtSeTe for 10 ps (time step:1 fs). Although the flexural distance of single-layer penta-PtXY has increased, their atomic skeletons are still well conserved during the whole process. Additionally, the alteration of free energy only indicates a slight behavior of oscillation. It indicates that the structures of penta-PtXY are still stable even at high temperatures, demonstrating that these single-layers remain free-standing 2D materials at high temperatures. Therefore, once the as-studied penta-PtXY single-layers are synthesized, they can be used as anti-high-temperature materials in extreme environments.

Anisotropic Mechanical and Auxetic Properties. Subsequently, we conducted an in-depth examination of the mechanical stability of penta-PtXY through calculations of elastic constants (C_{ij}, N/m), Young's modules (Y, N/m), and Poisson's ratio (υ) (as seen in Table 2). The elastic constants of the three structures suit the Born−Huang criteria[54] (C_{11}, C_{22}, C_{66} > 0 and $C_{11}C_{22}-C_{12}^2$ > 0) for penta-PtXY. The calculated values for penta-PtXY are as follows: C_{11} = 36.52, C_{22} = 64.26, C_{12} = 1.6, and C_{66} = 23.07 N/m, obtained by fitting the strain-dependent energy curve of the penta-PtXY single-layers. This confirms the satisfaction of the Born−Huang criteria.

Therefore, the 2D penta-PtXY monolayers are all mechanically stable. For 2D material, the in-plane Poisson's ratio (υ) and Young's modulus (E) can be depicted as the next formulas, where θ is an arbitrary direction angle relative to x-direction.[58]

$$Y(\theta) = \frac{C_{11}C_{22} - C_{12}^2}{C_{11}\sin^4\theta + C_{22}\cos^4\theta + \left(\frac{C_{11}C_{22}-C_{12}^2}{C_{66}} - 2C_{12}\right)\cos^4\theta\sin^4\theta}$$

and

https://doi.org/10.1021/acsomega.4c00803
ACS Omega 2024, 9, 32502−32512

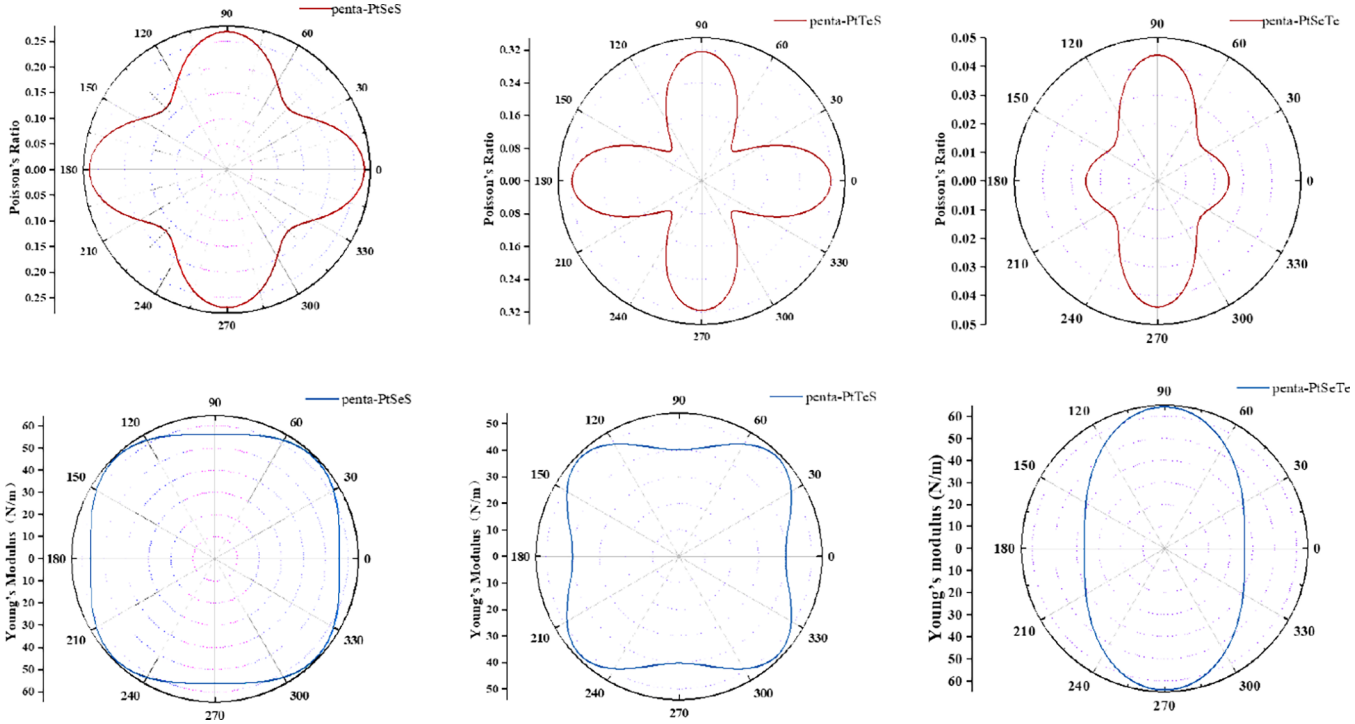

Figure 5. Poisson's ratio and Young's modulus of penta-PtXY.

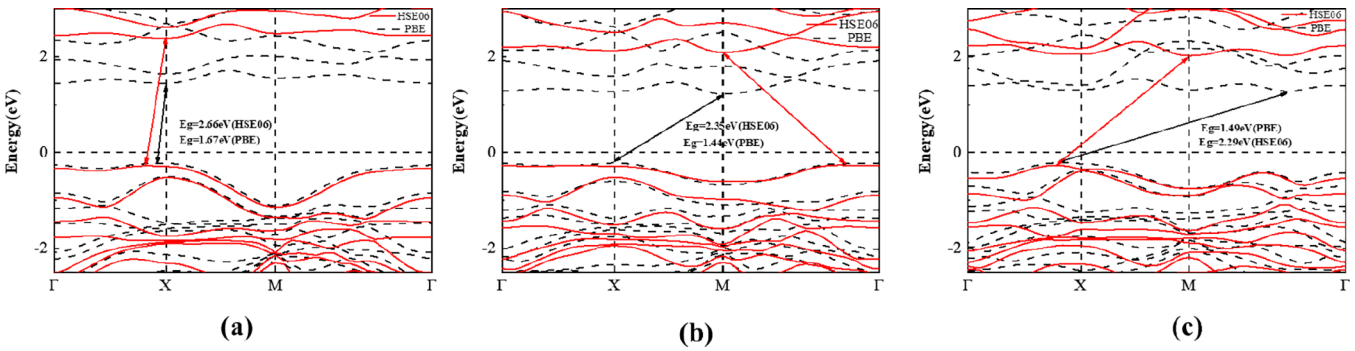

Figure 6. Band structures of the (a) penta-PtSeS, (b) penta-PtTeS, and (c) penta-PtSeTe monolayer (line: HSE06, dot line: PBE).

$$V(\theta) = \frac{\left(C_{11} + C_{22} - \frac{C_{11}C_{22} - C_{12}^2}{C_{66}}\right)\cos^4\theta \sin^4\theta - C_{11}(\sin^4\theta + \cos^4\theta)}{C_{11}\sin^4\theta + C_{22}\cos^4\theta + \left(\frac{C_{11}C_{22} - C_{12}^2}{C_{66}} - 2C_{12}\right)\cos^4\theta \sin^4\theta}$$

The in-plane Poisson's ratio (ν) and Young's modulus (E) are shown in Figure 5. It is observed that the Poisson's ratio and Young's modulus curve are nonround, indicating mechanical anisotropy in the penta-PtXY monolayer. The in-plane Young's modulus is up to the value of 63.86/52.59/64.19 N/m for the penta-PtSeS, penta-PtTeS, and penta-PtSeTe monolayers at θ = 45° and 90° (Y_{22}). And it reaches the minimum value of 56.21/40.21/36.48 N/m for the penta-PtSeS/penta-PtTeS/penta-PtSeTe monolayer at θ = 90° and 180° (Y_{11}). The anisotropic Young's modulus indicates that the penta-PtXY monolayers have significantly different deformation resistance in different directions. For the Poisson's ratio $\nu(\theta)$ of penta-PtXY monolayers, the in-plane anisotropy ratios are 1.59, 3.0, and 2.24 for penta-PtSeS, penta-PtTeS, and penta-PtSeTe monolayers, respectively. It can be seen that compared with the ones of graphene,[55] BN,[56] and pentagonal graphene,[57] the Young's moduli of penta-PtXY are significantly lower, demonstrating reduced stiffness and greater sensitivity to elastic deformation in the penta-PtXY single-layers (see Table 2). For penta-PtSeS, the Young's moduli is close to those of penta-P_2C (60.33 N·m^{-1}),[59] MnS(59.93 N·m^{-1}),[60] and penta-TiP (54.2 N·m^{-1}).[61] The Poisson's ratios ν are all lower than the ones of penta-P_2C (0.53)[59] and penta-TiP (0.478).[61]

Bonding Characteristics and Electronic Properties. When it refers to electronic properties, penta-PtXY monolayers are found to be indirect bandgap semiconductors (Figure 6). The bandgap values are 1.67 eV for penta-PtSeS, 1.44 eV for penta-PtTeS, and 1.49 eV for penta-PtSeTe based on GGA-PBE calculations (provided in Table 1). In general, the bandgaps of insulators and semiconductors have been severely underestimated under GGA-PBE[62] because of the absence of derivative discontinuity in the exchange-correlation functional. Therefore, we repeat the band structure by using the Heyd−Scuseria−Ernzerhof (HSE06) functional to compute more accurate band gap values. The bandgaps are 2.66, 2.35, and 2.29 eV for penta-PtSeS, penta-PtTeS, and penta-PtSeTe by HSE06 calculations, respectively, comparable to those of β-

https://doi.org/10.1021/acsomega.4c00803
ACS Omega 2024, 9, 32502−32512

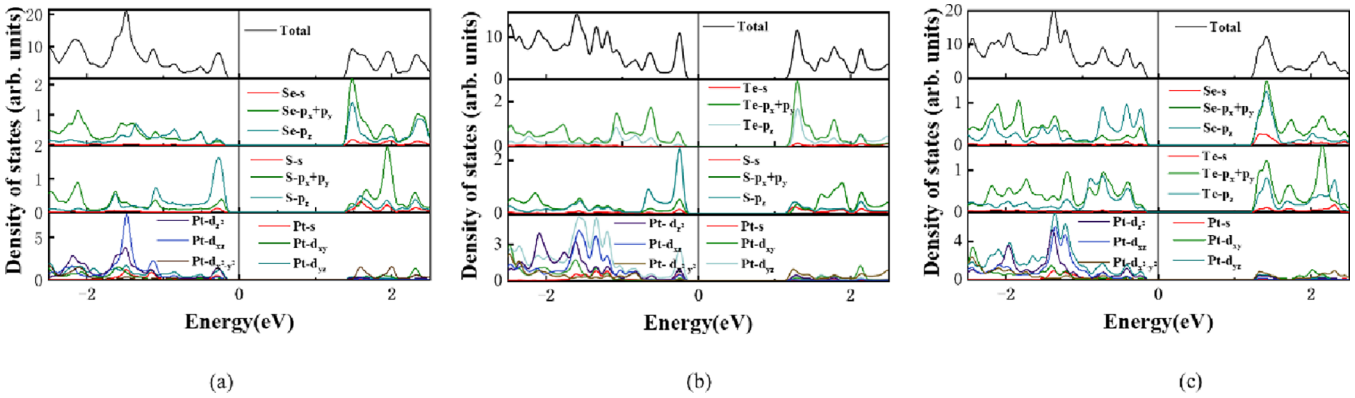

Figure 7. Total and partial DOS of (a) penta-PtSeS, (b) penta-PtTeS, and (c) penta-PtSeTe, based on the PBE calculation.

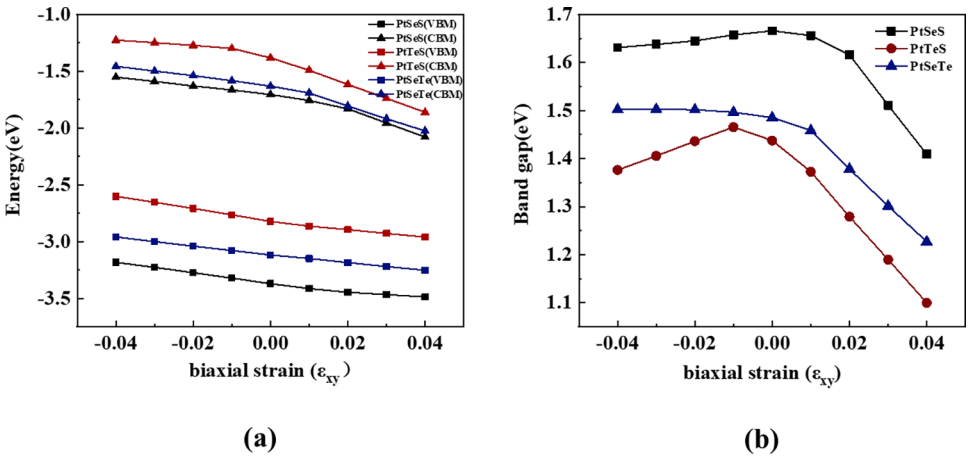

Figure 8. (a) Shifts in CBM and VBM and (b) band gaps of penta-PtXY monolayers depending on the biaxial strain, based on PBE calculations.

CdS_2(2.53 eV),[60] penta-PdSSe (2.34 eV),[63] penta-BNSi(2.21 eV),[21] and penta-CNP(2.62 eV).[24] According to Figure 6, it is observed that the CBM and VBM positions of the penta-PtXY monolayer in the band structure change. For example, the VBM of the penta-PtSeS monolayer shifts to the left, and the VBM of the penta-PtSeTe monolayer moves from point M to the one in the path M-Γ. It is considered that the PBE functional is a kind of exchange correlation functional in which the exchange correlation energy is discontinuous, while HSE06 is a mixed one, adding Hartree−Fock to the exchange correlation energy of a pure functional, which improves the description of electron correlation.[64−66] Therefore, HSE06 is a more precise method for the calculation of band structure.

We calculated the corresponding total and partial density of states (DOS) for the three monolayers (refer to Figure 7) to further explore the orbital contributions. The CBM and VBM of penta-PtSeS/penta-PtTeS both consist of Y-pz, Pt-dz^2 orbitals, and X-px+py orbitals. The VBM of the penta-PtSeTe monolayer consists of X-px+X-py and Pt-dyz orbitals. Clearly, two orbital hybrids are evident: one is X-px+X-py and Pt-dyz, and the other is Y-pz and Pt-dz^2. The robust orbital hybridizations between the transition metal and the sulfur group of elements in the penta-PtXY greatly raise their stability, just like the stability analysis above. In addition, to verify the analysis, a partial charge density was employed to gain a deeper understanding. The partial charge density is shown in Figure S3, which consists of the analysis of the part density of thestate distribution map above.

After considering the stability and electronic properties of penta-PtXY, it is inevitable to view the structural properties at outer strains because the strain is indispensable in material processing and growth.[67] To gain a profound understanding of the impact of different strains on the electronic properties of penta-PtXY single-layers, we investigated their band structures under biaxial strain influence from −4% to 4% under the PBE hybrid functional, in which the negative and positive values impose compression and extension formation. To verify their stabilities, we have calculated the phonon spectra of the penta-PtXY under ε_{xy} = −4% and ε_{xy} = −4%, as shown in Figure S4. The transformation of the penta-PtXY band structures with external strains (ε_{xy}) is elucidated in Figure S5. The energy evolutions of the VBM and CBM of penta-PtXY are shown in Figure 8a. From ε_{xy} = 0% to ε_{xy} = 4%, namely, during the process of applying extension biaxial strains, the eigenvalues of state VBM and CBM of penta-PtXY are always decreasing. Among them, the variation of the CBM energy level for penta-PtTeS is most obvious from −1.38 to −1.86 eV. While the eigenvalues of state VBM and CBM of penta-PtXY are both always slightly increased under the application of the compression biaxial strains (from ε_{xy} = 0% to ε_{xy} = −4%). The evolution of the band gaps under the strains is elucidated in Figure 8b. The band gap of the penta-PtSeS single-layer is observed to monotonically decrease with increasing compressive and tensile stress. Specifically, with an increasing compressive strain, the band gap gradually decreases. Employing a tensile strain of 1% results in a slow decrease in the band gap. However, as the tensile strain continues to increase to 4%,

https://doi.org/10.1021/acsomega.4c00803
ACS Omega 2024, 9, 32502−32512

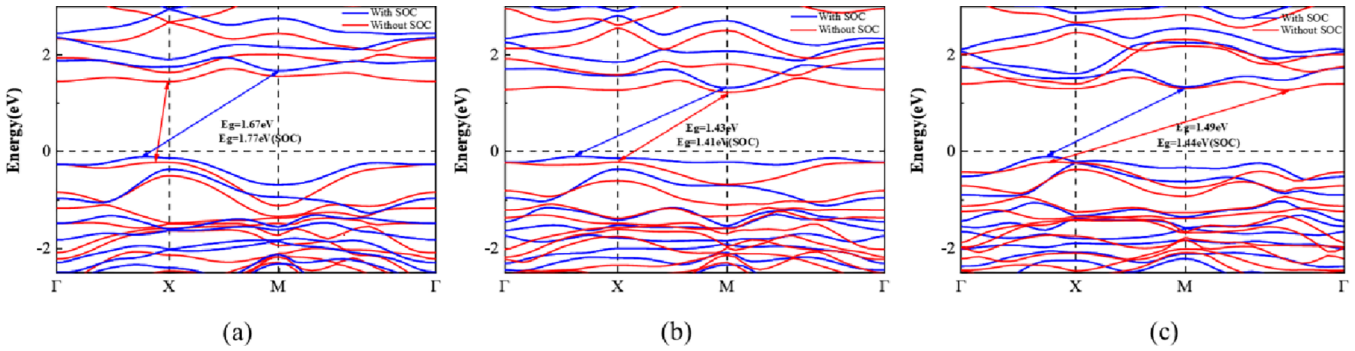

Figure 9. Band structures with and without SOC effect of (a) penta-PtSeS, (b) penta-PtTeS, and (c) penta-PtSeTe monolayers.

Table 3. Carrier Effective Masses (m^*/m_0), Deformation Potential Values E_{di} (eV), Elastic Constants C_{2D} (J m^{-2}), and Carrier Mobility μ_{2Di} (cm^2 V^{-1}s^{-1}) along the x and y Directions of the Penta-PtXY Monolayer

materials	carrier type	m_x^*/m_0	m_y^*/m_0	E_{dx} (eV)	E_{dy} (eV)	C_{2Dx} (J m^{-2})	C_{2Dy} (J m^{-2})	μ_{2Dx} (cm^2 V^{-1}s^{-1})	μ_{2Dy} (cm^2 V^{-1}s^{-1})	anisotropy ratio
penta-PtSeS	electron	3.04	0.73	1.65	3.58	59.46	83.53	102.72	127.6	1.24
	hole	1.49	2.68	1.78	2.96	59.46	83.53	133.65	37.8	3.54
penta-PtTeS	electron	0.51	1.2	6.53	7.59	44.98	69.85	55.97	27.44	2.04
	hole	1.16	1.07	1.26	3.01	44.98	69.85	461.2	136.17	3.39
penta-PtSeTe	electron	0.50	0.6	4.6	5.15	40.62	71.52	148.06	171.92	1.16
	hole	0.79	0.93	1.08	1.92	40.62	71.52	1087.7	518.06	2.10

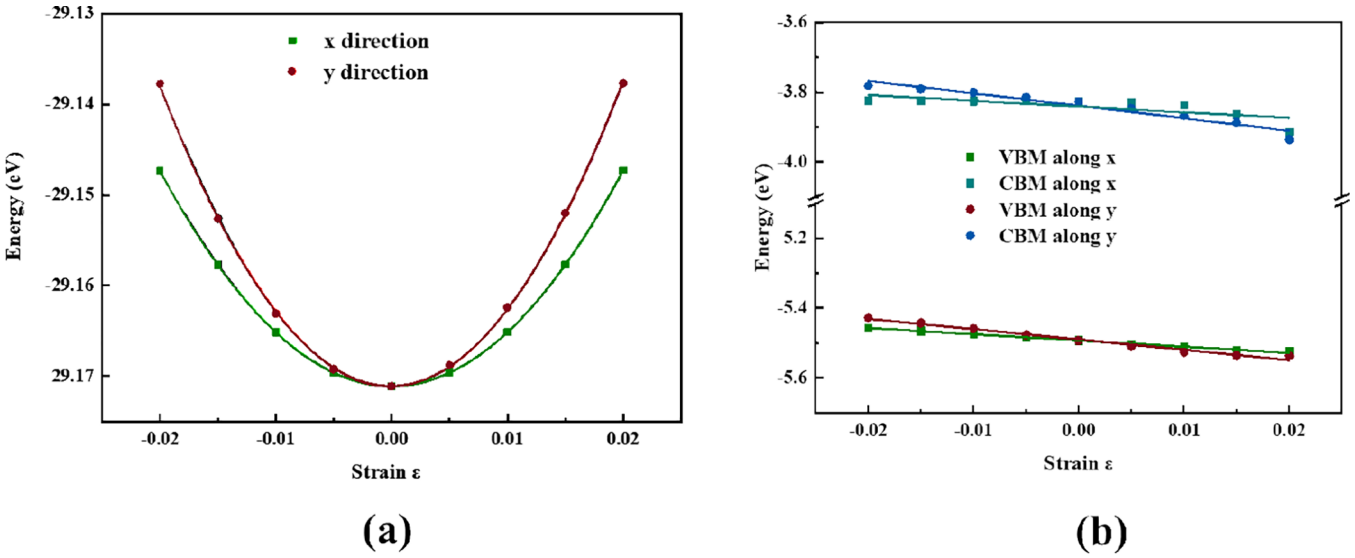

Figure 10. (a) Shifts in CBM and VBM versus the uniaxial strain applied in the x and y directions. Here, the vacuum level has been subtracted. (b) Computed strain−energy relations for the penta-PtSeS monolayer.

the band gap decreases dramatically to 1.41 eV. In the case of the penta-PtTeS monolayer, the band gap initially increases and then decreases, reaching a maximum under a compressive stress of 1%. Subsequently, the band gap sharply reduces under tensile strain, dropping to 1.01 eV under 4% strain. Unlike penta-PtSeS and penta-PtTeS monolayers, the bandgap of penta-PtSeTe increases progressively under the compressive stress. While the band gap drops dramatically under tensile stress, which is similar to penta-PtSeS and penta-PtTeS. It indicates a stronger mechanical stress reaction variability of penta-PtTeS among the three materials. To understand the mechanism behind the evolution of the band gap, the influence of the strain on the band structures has also been considered in Figure S5. In the strain range (−4% ∼ 4%), the penta-PtXY all exhibit indirect bandgap characteristics. In the case of penta-PtSeS and penta-PtTeS, under applied stress from −1% to 1%, the CBM shifts from point Γ to point M, and the VBM shifts from point X to point Γ. Meanwhile, for penta-PtSeTe, the VBM is in the Γ-X direction, and the CBM is in the M-Γ direction within the strain range of −4% to 4%. The corresponding response properties of the penta-PtXY monolayer may be helpful in strain engineering applications.

The impact of spin−orbit coupling (SOC) on the band structure is considered due to the incorporation of the heavy atomic mass of transition metal Pt. As shown in Figure 9, it can be observed that the electronic structure of the penta-PtXY monolayer is similar regardless of whether there is spin−orbit coupling (SOC) influence, and the band gaps of penta-PtTeS and penta-PtSeTe are slightly smaller when considering SOC. Moreover, the performance with or without SOC at the

https://doi.org/10.1021/acsomega.4c00803
ACS Omega 2024, 9, 32502−32512

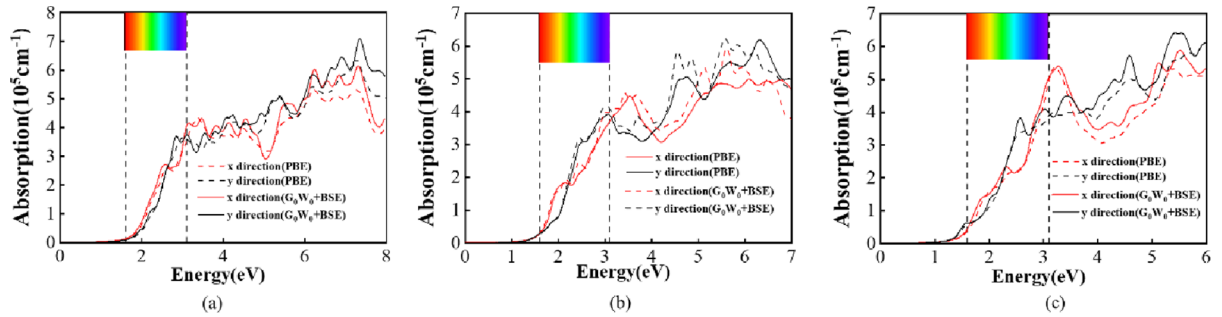

Figure 11. Light absorption of (a) penta-PtSeS, (b) penta-PtTeS, and (c) penta-PtSeTe monolayer calculated by the G_0W_0+BSE method and PBE method.

valence band is almost the same properties near the Γ points, while the conduction band is different near the Γ point.

Anisotropic Carrier Mobility. In addition, carrier mobility also has a significant impact on 2D semiconductor applications, besides electronic bandgap and VBM/CBM energy levels.[68,69] Here, based on the theory of deformed potential energy,[70] the carrier mobility of the penta-PtXY has been calculated[71,72] following the formula $\mu_{2D} = \frac{e\hbar^3 C_{2D}}{k_B T m^* \bar{m} E_d^2}$ where e, $\hbar$, C_{2D}, T, k_B, $\bar{m}$, m^*, E_d, and μ_{2D} represent electron charge, reduced Planck's constant, elastic modulus, temperature (set to be 300 K), Boltzmann's constant, average effective mass ($\bar{m} = \sqrt{m_x^* m_y^*}$), effective mass, deformation potential constant, and carrier mobility, respectively.

As can be seen from Figure 6a, the band dispersion near the CBM point in the y direction (X-M) is notably steeper than that in the x direction (X-Γ). Similarly, as can be seen from Figure 6b, the band dispersion near the VBM point in the y direction (X-M) is notably steeper than that in the x direction (X-Γ). Also, the carrier effective masses $m^* = h^2\left[\frac{\partial^2 E(k)}{\partial k^2}\right]^{-1}$ determined by the band dispersion of the CBM or VBM valley show a noticeable anisotropy due to the different dispersions between CBM and VBM in band structures. The effective mass of electrons and holes in the penta-PtXY monolayer is presented in Table 3. It can be seen that the effective mass of electrons for the penta-PtSeS single-layer in the x direction (3.04 me) is much larger than that in the y direction (0.79 me). While the effective mass of holes in the y direction (2.68 me) is higher than that in the x direction (1.49 me). For the penta-PtSeTe monolayers, all of the effective masses in the x direction are smaller than those in the y direction.

On the basis of the deformation potential theory, the carrier mobility of 2D materials can be estimated with the known deformation potential (DP) constants (E) and the 2D elastic moduli (C_{2D}). As shown in Figure 10b and Figure S6c,d, the band edges of the CBM and VBM decrease quasilinearly with the strain in the x or y directions but show a marked difference in the magnitude of the slope. For both penta-PtXY monolayers (Figure 10a and Figures S6a,b), the computed elastic moduli in the y direction are much higher than those in the x direction, suggesting high anisotropy in mechanical properties. As shown in Table 3, the predicted hole mobilities of the penta-PtSeTe single-layer in x and y directions come up to 1.09×10^3 and 0.52×10^3 cm^2 V^{-1}s^{-1}, respectively, about 1 orders of magnitude higher than that (<100 cm^{2}V^{-1}s^{-1}) of the MoS_2 monolayer.[73] Notably, the ratios [max (μ_x, μ_y)/min (μ_x, μ_y)] of hole mobilities of the penta-PtSeS, penta-PtTeS, and penta-PtSeTe monolayers amount to 3.54, 3.39, and 2.10, respectively, showing very significant hole mobility anisotropy. The high anisotropy ratio improves the sensitivity of polarized nanodevices.

Anisotropic Optical Properties. The appropriate band gap (2.29−2.66 eV) of the penta-PtXY single-layer demonstrates that it may show an ideal optical absorption.[74] Here, we have calculated the optical absorbance of the penta-PtXY single-layer under the PBE functional to visualize their light-harvesting performance (illustrated in Figure 11 (dotted lines)). It is worth noting that the light absorption of penta-PtSeS/penta-PtSeTe in the y direction is slightly greater than that in the x direction when the energy is greater than 4 eV/3.5 eV. It shows the three penta-PtXY monolayers are all in-plane anisotropic in optical properties, which is a prerequisite for polarization-sensitive device applications. In addition, it is observed from Figure 10 that the absorption coefficient of the penta-PtXY monolayer can reach up to 10^5 cm^{-1} from the visible region to the ultraviolet one, which is comparable to those of some metal-free photocatalysts.[75] In particular, the light absorption of penta-PtSeTe in the visible range can reach 5×10^5 cm^{-1} in the x direction. They are 1.3 and 1.25 times higher than the monolayers of penta-PtSeS and penta-PtTeS, slightly higher than the monolayer MoS_2 (4.7×10^5 cm^{-1})[76,77] and much higher than the monolayers t-ZnS[78] and BiOI.[79]

To acquire more precise optical absorption characteristics, we have calculated the light absorption spectra of the penta-PtXY as shown in Figure 11(solid line) by the G_0W_0+BSE method[80,81] (the G_0W_0 method takes into account the multibody interaction through the quasi-particle method, and the BSE equation incorporates electron−hole interaction). We have found that the light absorption spectrum is similar to the spectrum estimated by the PBE method. The first absorption peaks of the three penta-PtXY monolayers are all red-shifted, and the smaller optical bandgaps are obtained by G_0W_0+BSE. The absorption peaks in visible light are all slightly higher than those obtained by the PBE calculation method. The absorption peaks are stronger in the ultraviolet region. The outcomes indicate that penta-PtXY materials are more advantageous in optoelectronic devices. In addition, the anisotropy ratios in the x and y directions reached 1.56, 2.08, and 2.11 for the penta-PtSeS, penta-PtTeS, and penta-PtSeTe monolayers, respectively. Furthermore, to understand the influence of the strain on the light absorption properties, the light absorption properties have been calculated under biaxial strain based on PBE functionals, as seen in Figure S7. It is seen that the absorption peak of the penta-PtXY single-layers is all red-shifted in the visible range and increases in the UV region at the strain range from −4% to 4%.

https://doi.org/10.1021/acsomega.4c00803
ACS Omega 2024, 9, 32502−32512

CONCLUSIONS

In summary, we have designed a family of 2D semiconducting monolayers, penta-PtXY, with anisotropic physical properties. The penta-PtXY single-layer presents an indirect-gap semiconducting characteristic with a bandgap of 2.39−2.66 eV. The penta-PtXY single-layers possess high mechanical anisotropy and an appropriate in-plane Poisson's ratio. The single-layers hold a large hole mobility anisotropic ratio of 3.54, 3.39, and 2.10 for penta-PtSeS, penta-PtTeS, and penta-PtSeTe, individually, demonstrating a high hole mobility anisotropy. In particular, the relatively high hole mobility (1.09×10^3 $cm^2 V^{-1}s^{-1}$) of the penta-PtSeTe single-layer allows its potential application in 2D FETs. Finally, G_0W_0+BSE calculations show that the monolayer also has significant optical anisotropy with maximum anisotropy ratios of 1.56 for penta-PtSeS, 2.08 for penta-PtTeS, and 2.11 for penta-PtSeTe. The highest absorptivities are 6.45×10^5 cm^{-1} for penta-PtSeS, 6.22×10^5 cm^{-1} for penta-PtTeS, and 6.41×10^5 cm^{-1} for penta-PtSeTe. The penta-PtXY monolayers with anisotropic optical, electronic, and mechanical properties have enormous application potential in the field of polarization-sensitive devices.

ASSOCIATED CONTENT

Supporting Information

The Supporting Information is available free of charge at https://pubs.acs.org/doi/10.1021/acsomega.4c00803.

Penta-PtXY antioxidant and partial charge density; phonon spectrum, energy band, and light absorption after strain application; carrier mobility data and cell data (PDF)

AUTHOR INFORMATION

Corresponding Authors

Cuixia Yan − *Faculty of Materials Science and Engineering, Kunming University of Science and Technology, Kunming 650093, People's Republic of China;* orcid.org/0000-0001-5766-1254; Email: cuixiayan@kust.edu.cn

Jinming Cai − *Faculty of Materials Science and Engineering, Kunming University of Science and Technology, Kunming 650093, People's Republic of China; Southwest United Graduate School, Kunming 650000, People's Republic of China;* orcid.org/0000-0003-0869-1515; Email: j.cai@kust.edu.cn

Authors

Ting Yang − *Faculty of Materials Science and Engineering, Kunming University of Science and Technology, Kunming 650093, People's Republic of China*

Shi Qiu − *Faculty of Materials Science and Engineering, Kunming University of Science and Technology, Kunming 650093, People's Republic of China*

Yanghao Tang − *Faculty of Materials Science and Engineering, Kunming University of Science and Technology, Kunming 650093, People's Republic of China*

Ao Du − *Faculty of Materials Science and Engineering, Kunming University of Science and Technology, Kunming 650093, People's Republic of China*

Complete contact information is available at: https://pubs.acs.org/10.1021/acsomega.4c00803

Author Contributions

C.Y. contributed to the conception of the study; T.Y. performed the calculations and manuscript writing, and C.Y. supervised the data analysis and manuscript revision; S.Q. contributed to data analysis with constructive discussions; Y.T. and A.D. contributed to data analysis with constructive discussions. J.C. provided equipment support.

Notes

The authors declare no competing financial interest.

ACKNOWLEDGMENTS

This work was supported by the National Natural Science Foundation of China (No. 12064020, 22372074, 62301240, 62271238), the Yunnan Fundamental Research Projects (Nos. 202301AW070017, 202201AT070078, 202201BE070001-009, 202201BE070001-017, 202101AV070008, 202101AW070010 and 202101AU070043), the Major Basic Research Project of Science and Technology of Yunnan (202302AG050007), Yunnan Innovation Team of Graphene Mechanism Research and Application Industrialization (202305AS350017), Graphene Application and Engineering Research Center of Education Department of Yunnan Providence (KKPP202351001), and Yanglei Academician Expert Workstation of Yunnan Province (202205AF15025). Numerical computations were performed on Hefei Advanced Computing Center.

REFERENCES

(1) Zhong, M.; Meng, H.; Liu, S.; Yang, H.; Shen, W.; Hu, C.; Yang, J.; Ren, Z.; Li, B.; Liu, Y.; He, J.; Xia, Q.; Li, J.; Wei, Z. In-Plane Optical and Electrical Anisotropy of 2D Black Arsenic. *ACS Nano* **2021**, *15* (1), 1701−1709.

(2) Wang, Y.; Qiu, G.; Wang, R.; Huang, S.; Wang, Q.; Liu, Y.; Du, Y.; Goddard, W. A.; Kim, M. J.; Xu, X.; Ye, P. D.; Wu, W. Field-Effect Transistors Made from Solution-Grown Two-Dimensional Tellurene. *Nature Electronics* **2018**, *1* (4), 228−236.

(3) Li, L.; Wang, W.; Gong, P.; Zhu, X.; Deng, B.; Shi, X.; Gao, G.; Li, H.; Zhai, T. 2D Gep: An Unexploited Low-Symmetry Semiconductor with Strong in-Plane Anisotropy. *Adv. Mater.* **2018**, *30* (14), No. 1706771.

(4) Yang, Y.; Liu, S.-C.; Wang, Y.; Long, M.; Dai, C.-M.; Chen, S.; Zhang, B.; Sun, Z.; Sun, Z.; Hu, C.; Zhang, S.; Tong, L.; Zhang, G.; Xue, D.-J.; Hu, J.-S. In-Plane Optical Anisotropy of Low-Symmetry 2D GeSe. *Adv. Opt. Mater.* **2019**, *7* (4), No. 1801311.

(5) Shu, H. Highly-Anisotropic Carrier Transport and Optical Properties of Two-Dimensional Titanium Trisulfide. *J. Mater. Sci.* **2022**, *57* (5), 3486−3496.

(6) Li, L.; Gong, P.; Wang, W.; Deng, B.; Pi, L.; Yu, J.; Zhou, X.; Shi, X.; Li, H.; Zhai, T. Strong in-Plane Anisotropies of Optical and Electrical Response in Layered Dimetal Chalcogenide. *ACS Nano* **2017**, *11* (10), 10264−10272.

(7) Lai, J.; Liu, Y.; Ma, J.; Zhuo, X.; Peng, Y.; Lu, W.; Liu, Z.; Chen, J.; Sun, D. Broadband Anisotropic Photoresponse of the "Hydrogen Atom" Version Type-Ii Weyl Semimetal Candidate $TaIrTe_4$. *ACS Nano* **2018**, *12* (4), 4055−4061.

(8) Li, P.; Xu, Y.; Liang, C.; Zeng, X. C. $MgXN_2$ (X = Hf/Zr) Monolayers: Auxetic Semiconductor with Highly Anisotropic Optical/Mechanical Properties and Carrier Mobility. *J. Phys. Chem. Lett.* **2022**, *13* (45), 10534−10542.

(9) Su, J. W.; Shen, W. F.; Chen, J. Z.; Yang, S. J.; Liu, J.; Feng, X.; Zhao, Y. H.; Hu, C. G.; Li, H. Q.; Zhai, T. Y. 2D Ternary Vanadium Phosphorous Chalcogenide with Strong in-Plane Optical Anisotropy. *Inorganic Chemistry Frontiers* **2021**, *8* (12), 2999−3006.

(10) Xia, F.; Wang, H.; Jia, Y. Rediscovering Black Phosphorus as an Anisotropic Layered Material for Optoelectronics and Electronics. *Nat. Commun.* **2014**, *5* (1), 4458.

(11) Wang, H.; Chen, M. L.; Zhu, M.; Wang, Y.; Dong, B.; Sun, X.; Zhang, X.; Cao, S.; Li, X.; Huang, J.; Zhang, L.; Liu, W.; Sun, D.; Ye, Y.; Song, K.; Wang, J.; Han, Y.; Yang, T.; Guo, H.; Qin, C.; Xiao, L.; Zhang, J.; Chen, J.; Han, Z.; Zhang, Z. Gate Tunable Giant Anisotropic Resistance in Ultra-Thin Gate. *Nat. Commun.* **2019**, *10* (1), 2302.
(12) Liu, F. C.; Zheng, S. J.; He, X. X.; Chaturvedi, A.; He, J. F.; Chow, W. L.; Mion, T. R.; Wang, X. L.; Zhou, J. D.; Fu, Q. D.; Fan, H. J.; Tay, B. K.; Song, L.; He, R. H.; Kloc, C.; Ajayan, P. M.; Liu, Z. Highly Sensitive Detection of Polarized Light Using Anisotropic 2D ReS_2. *Adv. Funct. Mater.* **2016**, *26* (8), 1169−1177.
(13) Zhang, E.; Wang, P.; Li, Z.; Wang, H.; Song, C.; Huang, C.; Chen, Z.-G.; Yang, L.; Zhang, K.; Lu, S.; Wang, W.; Liu, S.; Fang, H.; Zhou, X.; Yan, H.; Zou, J.; Wan, X.; Zhou, P.; Hu, W.; Xiu, F. Tunable Ambipolar Polarization-Sensitive Photodetectors Based on High-Anisotropy $ReSe_2$ Nanosheets. *ACS Nano* **2016**, *10* (8), 8067−8077.
(14) Shangguan, W.; Yan, C. X.; Li, W. Q.; Long, C.; Liu, L. M.; Qi, C. C.; Li, Q. Y.; Zhou, Y.; Guan, Y. R.; Gao, L.; Cai, J. M. Two-Dimensional Semiconductor Materials with High Stability and Electron Mobility in Group-11 Chalcogenide Compounds: MnX (M = Cu, Ag, Au; N = Cu, Ag, Au; X = S, Se, Te; M ≠ N). *Nanoscale* **2022**, *14* (11), 4271−4280.
(15) Shangguan, W.; Yan, C.; Cai, J. Quasi-Planar Tetracoordiante Carbon Networks with Tunable Electronic Properties Combined with Ultra-High Carrier Mobility and Optical Absorption Coefficient: Two-Dimensional Be_2C. *Appl. Surf. Sci.* **2022**, *604*, No. 154644.
(16) Li, P.; Zhang, J.; Zhu, C.; Shen, W.; Hu, C.; Fu, W.; Yan, L.; Zhou, L.; Zheng, L.; Lei, H.; Liu, Z.; Zhao, W.; Gao, P.; Yu, P.; Yang, G. Penta-PdPSe: A New 2D Pentagonal Material with Highly in-Plane Optical, Electronic, and Optoelectronic Anisotropy. *Adv. Mater.* **2021**, *33* (35), No. 2102541.
(17) Oyedele, A. D.; Yang, S.; Liang, L.; Puretzky, A. A.; Wang, K.; Zhang, J.; Yu, P.; Pudasaini, P. R.; Ghosh, A. W.; Liu, Z.; Rouleau, C. M.; Sumpter, B. G.; Chisholm, M. F.; Zhou, W.; Rack, P. D.; Geohegan, D. B.; Xiao, K. $Pdse_2$: Pentagonal Two-Dimensional Layers with High Air Stability for Electronics. *J. Am. Chem. Soc.* **2017**, *139* (40), 14090−14097.
(18) Gu, Y.; Cai, H.; Dong, J.; Yu, Y.; Hoffman, A. N.; Liu, C.; Oyedele, A. D.; Lin, Y. C.; Ge, Z.; Puretzky, A. A.; Duscher, G.; Chisholm, M. F.; Rack, P. D.; Rouleau, C. M.; Gai, Z.; Meng, X.; Ding, F.; Geohegan, D. B.; Xiao, K. Two-Dimensional Palladium Diselenide with Strong in-Plane Optical Anisotropy and High Mobility Grown by Chemical Vapor Deposition. *Adv. Mater.* **2020**, *32* (19), No. 1906238.
(19) Duan, R.; He, Y.; Zhu, C.; Wang, X.; Zhu, C.; Zhao, X.; Zhang, Z.; Zeng, Q.; Deng, Y.; Xu, M.; Liu, Z. 2D Cairo Pentagonal Pdps: Air-Stable Anisotropic Ternary Semiconductor with High Optoelectronic Performance. *Adv. Funct. Mater.* **2022**, *32* (21), No. 2113255.
(20) Wang, C.; Zhou, X.; Li, Y. Penta-Bcn Monolayer: A Metal-Free Photocatalyst with a High Carrier Mobility for Water Splitting. *Phys. Chem. Chem. Phys.* **2022**, *24* (43), 26863−26869.
(21) Varjovi, M. J.; Kilic, M. E.; Durgun, E. Ternary Pentagonal Bnsi Monolayer: Two-Dimensional Structure with Potentially High Carrier Mobility and Strong Excitonic Effects for Photocatalytic Applications. *Physical Review Materials* **2022**, *6* (3), No. 034004.
(22) Mao, Y.; Zhang, J.; Bai, S.; Wu, M.; Luo, D.; Tang, S. The Electronic, Mechanical Properties and in-Plane Negative Poisson's Ratio in Novel Pentagonal NiX_2 (X = S, Se, Te) Monolayers with Strong Anisotropy: A First-Principles Prediction. *Comput. Mater. Sci.* **2023**, *216*, No. 111873.
(23) Shen, Y. H.; Sun, J.; Chen, Y. Y.; Ni, D. Y.; Li, T. W.; Yoshikawa, A.; Kawazoe, Y.; Wang, Q. Penta-OsP_2 and Penta-Rhs_2 Sheets Derived from Marcasite and Pyrite with Low Lattice Thermal Conductivity. *Journal of Materials Chemistry A* **2022**, *10* (40), 21356−21367.
(24) Sun, W.; Shen, Y.; Guo, Y.; Chen, Y.; Wang, Q. 1,2,4-Azadiphosphole-Based Piezoelectric Penta-CNP Sheet with High Spontaneous Polarization. *Appl. Surf. Sci.* **2021**, *554*, No. 149499.
(25) Sharma, S. B.; Qattan, I. A.; Kc, S.; Alsaad, A. M. Large Negative Poisson's Ratio and Anisotropic Mechanics in New Penta-PBN Monolayer. *ACS Omega* **2022**, *7* (41), 36235−36243.
(26) Long, C.; Liang, Y.; Jin, H.; Huang, B. B.; Dai, Y. PdSe: Flexible Two-Dimensional Transition Metal Dichalcogenides Monolayer for Water Splitting Photocatalyst with Extremely Low Recombination Rate. *ACS Applied Energy Materials* **2019**, *2* (1), 513−520.
(27) Gao, Y.; Liu, X.; Hu, W.; Yang, J. Tunable N-Type and P-Type Doping of Two-Dimensional Layered $Pdse_2$via Organic Molecular Adsorption. *Phys. Chem. Chem. Phys.* **2020**, *22* (23), 12973−12979.
(28) Qin, D.; Yan, P.; Ding, G.; Ge, X.; Song, H.; Gao, G. Monolayer $PdSe_2$: A Promising Two-Dimensional Thermoelectric Material. *Sci. Rep.* **2018**, *8* (1), 2764.
(29) Lan, Y.-S.; Chen, X.-R.; Hu, C.-E.; Cheng, Y.; Chen, Q.-F. Penta-PdX_2 (X = S, Se, Te) Monolayers: Promising Anisotropic Thermoelectric Materials. *Journal of Materials Chemistry A* **2019**, *7* (18), 11134−11142.
(30) Cheng, P. K.; Liu, S.; Ahmed, S.; Qu, J.; Qiao, J.; Wen, Q.; Tsang, Y. H. Ultrafast Yb-Doped Fiber Laser Using Few Layers of PdS_2 Saturable Absorber. *Nanomaterials* **2020**, *10* (12), 2441.
(31) Zhang, L.; Zhang, C. W.; Zhang, S. F.; Ji, W. X.; Li, P.; Wang, P. J. Two-Dimensional Honeycomb-Kagome Ta_2S_3: A Promising Single-Spin Dirac Fermion and Quantum Anomalous Hall Insulator with Half-Metallic Edge States. *Nanoscale* **2019**, *11* (12), 5666−5673.
(32) Naseri, M. First-Principles Prediction of a Novel Cadmium Disulfide Monolayer (Penta-CdS_2): Indirect to Direct Band Gap Transition by Strain Engineering. *Chem. Phys. Lett.* **2017**, *685*, 310−315.
(33) Gu, Y.; Zhang, L.; Cai, H.; Liang, L.; Liu, C.; Hoffman, A.; Yu, Y.; Houston, A.; Puretzky, A. A.; Duscher, G.; Rack, P. D.; Rouleau, C. M.; Meng, X.; Yoon, M.; Geohegan, D. B.; Xiao, K. Stabilized Synthesis of 2D Verbeekite: Monoclinic $PdSe_2$ Crystals with High Mobility and in-Plane Optical and Electrical Anisotropy. *ACS Nano* **2022**, *16* (9), 13900−13910.
(34) Kresse, G.; Furthmüller, J. Efficient Iterative Schemes for Ab Initio Total-Energy Calculations Using a Plane-Wave Basis Set. *Phys. Rev. B* **1996**, *54* (16), 11169−11186.
(35) Kresse, G.; Furthmüller, J. J. C. m. s. Efficiency of Ab-Initio Total Energy Calculations for Metals and Semiconductors Using a Plane-Wave Basis Set. *Comput. Mater. Sci.* **1996**, *6* (1), 15−50.
(36) Perdew, J. P.; Burke, K.; Ernzerhof, M. J. P. r. l. Generalized Gradient Approximation Made Simple. *Phys. Rev. Lett.* **1996**, *77* (18), 3865.
(37) Krukau, A. V.; Vydrov, O. A.; Izmaylov, A. F.; Scuseria, G. E. Influence of the Exchange Screening Parameter on the Performance of Screened Hybrid Functionals. *J. Chem. Phys.* **2006**, *125* (22), No. 224106.
(38) Blöchl, P. E. Projector Augmented-Wave Method. *Phys. Rev. B* **1994**, *50* (24), 17953−17979.
(39) Kresse, G.; Joubert, D. From Ultrasoft Pseudopotentials to the Projector Augmented-Wave Method. *Phys. Rev. B* **1999**, *59* (3), 1758−1775.
(40) Monkhorst, H. J.; Pack, J. D. Special Points for Brillouin-Zone Integrations. *Phys. Rev. B* **1976**, *13* (12), 5188−5192.
(41) Togo, A.; Oba, F.; Tanaka, I. First-Principles Calculations of the Ferroelastic Transition between Rutile-Type and $CaCl_2$ -Type SiO_2 at High Pressures. *Phys. Rev. B* **2008**, *78* (13), No. 134106.
(42) Zhang, S.; Zhou, J.; Wang, Q.; Chen, X.; Kawazoe, Y.; Jena, P. Penta-Graphene: A New Carbon Allotrope. *Proc. Natl. Acad. Sci.* **2015**, *112* (8), 2372−2377.
(43) Liu, J.; Zhang, X.; Wang, J.; Gu, L.; Chu, P. K.; Yu, X.-F. Global Structure Search for New 2D PtSSe Allotropes and Their Potential for Thermoelectirc and Piezoelectric Applications. *Chem. Phys. Lett.* **2022**, *805*, No. 139913.
(44) Yuan, Y.-X.; Pan, L.; Wang, Z.-Q.; Zeng, Z.-Y.; Geng, H.-Y.; Chen, X.-R. Two-Dimensional Janus Pentagonal MSeTe (M = Ni, Pd, Pt): Promising Water-Splitting Photocatalysts and Optoelectronic Materials. *Phys. Chem. Chem. Phys.* **2023**, *25* (38), 26152−26163.

https://doi.org/10.1021/acsomega.4c00803
ACS Omega 2024, 9, 32502−32512

(45) Bafekry, A.; Fadlallah, M. M.; Faraji, M.; Hieu, N. N.; Jappor, H. R.; Stampfl, C.; Ang, Y. S.; Ghergherehchi, M. Puckered Penta-Like PdPX (X = O, S, Te) Semiconducting Nanosheets: First-Principles Study of the Mechanical, Electro-Optical, and Photocatalytic Properties. *ACS Appl. Mater. Interfaces* **2022**, *14* (18), 21577−21584.
(46) Jiang, X. A.; Zhang, G. H.; Yi, W. C.; Yang, T.; Liu, X. B. Penta-BeP_2 Monolayer: A Superior Sensor for Detecting Toxic Gases in the Air with Excellent Sensitivity, Selectivity, and Reversibility. *ACS Appl. Mater. Interfaces* **2022**, *14* (30), 35229−35236.
(47) Shin, H.; Kang, S.; Koo, J.; Lee, H.; Kim, J.; Kwon, Y. Cohesion Energetics of Carbon Allotropes: Quantum Monte Carlo Study. *J. Chem. Phys.* **2014**, *140* (11), No. 114702.
(48) Liu, Z.; Wang, H. D.; Sun, J. Y.; Sun, R. J.; Wang, Z. F.; Yang, J. L. Penta-PtN: An Ideal Two-Dimensional Material for Nanoelectronics. *Nanoscale* **2018**, *10* (34), 16169−16177.
(49) Zhang, C.; Liu, J.; Shen, H.; Li, X.-Z.; Sun, Q. Identifying the Ground State Geometry of a MoN_2 Sheet through a Global Structure Search and Its Tunable P-Electron Half-Metallicity. *Chem. Mater.* **2017**, *29* (20), 8588−8593.
(50) Luo, W.; Xiang, H. Two-Dimensional Phosphorus Oxides as Energy and Information Materials. *Angew. Chem.* **2016**, *55* (30), 8575−8580.
(51) Huang, L.-F.; Gong, P.-L.; Zeng, Z. Phonon Properties, Thermal Expansion, and Thermomechanics of Silicene and Germanene. *Phys. Rev. B* **2015**, *91* (20), No. 205433.
(52) Maultzsch, J.; Reich, S.; Thomsen, C.; Requardt, H.; Ordejón, P. Phonon Dispersion in Graphite. *Phys. Rev. Lett.* **2004**, *92* (7), No. 075501.
(53) Yuan, J.-H.; Song, Y.-Q.; Chen, Q.; Xue, K.-H.; Miao, X.-S. Single-Layer Planar Penta-X_2N_4 (X = Ni, Pd and Pt) as Direct-Bandgap Semiconductors from First Principle Calculations. *Appl. Surf. Sci.* **2019**, *469*, 456−462.
(54) Qin, G.; Yan, Q.-B.; Qin, Z.; Yue, S.-Y.; Hu, M.; Su, G. Anisotropic Intrinsic Lattice Thermal Conductivity of Phosphorene from First Principles. *Phys. Chem. Chem. Phys.* **2015**, *17* (7), 4854−4858.
(55) Molina-Sánchez, A.; Wirtz, L. Phonons in Single-Layer and Few-Layer MoS_2 and WS_2. *Phys. Rev. B* **2011**, *84* (15), No. 155413.
(56) Ding, Y.; Wang, Y. Density Functional Theory Study of the Silicene-Like Six and XSi_3 (X = B, C, N, Al, P) Honeycomb Lattices: The Various Buckled Structures and Versatile Electronic Properties. *J. Phys. Chem. C* **2013**, *117* (35), 18266−18278.
(57) Zhang, S.; Zhou, J.; Wang, Q.; Chen, X.; Kawazoe, Y.; Jena, P. Penta-Graphene: A New Carbon Allotrope. *Proc. Natl. Acad. Sci. U.S.A.* **2015**, *112* (8), 2372−2377.
(58) Song, B.; Zhou, Y.; Yang, H.-M.; Liao, J.-H.; Yang, L.-M.; Yang, X.-B.; Ganz, E. Two-Dimensional Anti-Van't Hoff/Le Bel Array Alb_6 with High Stability, Unique Motif, Triple Dirac Cones, and Superconductivity. *J. Am. Chem. Soc.* **2019**, *141* (8), 3630−3640.
(59) Zhang, H.; Wang, X.; Zhou, P.; Ma, Z.; Sun, L. Two-Dimensional Ferromagnetic Chern Insulator: WSe_2 Monolayer. *Phys. Lett. A* **2021**, *402*, No. 127344.
(60) Lv, X.; Yu, L.; Li, F.; Gong, J.; He, Y.; Chen, Z. Penta-MS_2 (M = Mn, Ni, Cu/Ag and Zn/Cd) Monolayers with Negative Poisson's Ratios and Tunable Bandgaps as Water-Splitting Photocatalysts. *Journal of Materials Chemistry A* **2021**, *9* (11), 6993−7004.
(61) Ying, Y.; Fan, K.; Luo, X.; Huang, H. Predicting Two-Dimensional Pentagonal Transition Metal Monophosphides for Efficient Electrocatalytic Nitrogen Reduction. *Journal of Materials Chemistry A* **2019**, *7* (18), 11444−11451.
(62) Liu, F.; Ming, P.; Li, J. Ab Initio Calculation of Ideal Strength and Phonon Instability of Graphene under Tension. *Phys. Rev. B* **2007**, *76* (6), No. 064120.
(63) Zhou, Y.; Yang, X.; He, J. Pdsse: Two-Dimensional Pentagonal Janus Structures with Strong Visible Light Absorption for Photovoltaic and Photocatalytic Applications. *Vacuum* **2020**, *181*, No. 109649.
(64) Qi, C.; Yan, C.; Li, Q.; Yang, T.; Qiu, S.; Cai, J. Two-Dimensional Janus Chalcogenides: Candidates for Efficient Photocatalysts and Piezoelectric Materials. *Journal of Materials Chemistry A* **2024**, *12* (6), 3542−3556.
(65) Qi, C. C.; Yan, C. X.; Li, Q. Y.; Yang, T.; Qiu, S.; Cai, J. M. Two-Dimensional Janus Monolayers Al_2XYZ (X/Y/Z = S, Se, Te, X Not Equal Y Not Equal Z): First-Principles Insight into the Photocatalytic and Highly Adjustable Piezoelectric Properties. *Journal of Materials Chemistry C* **2023**, *11* (9), 3262−3274.
(66) Yuan, G.; Ma, X.; Liao, J.; Xie, T.; Xie, Q.; Yuan, Z. First-Principles Calculations of 2D Janus $WsSIn_2$monolayer for Photocatalytic Water Splitting. *ACS Applied Nano Materials* **2023**, *6* (3), 1956−1964.
(67) Yuan, J. H.; Yu, N. N.; Xue, K. H.; Miao, X. S. Ideal Strength and Elastic Instability in Single-Layer 8-Pmmn Borophene. *Rsc Advances* **2017**, *7* (14), 8654−8660.
(68) Kou, L.; Li, C.; Zhang, Z.-Y.; Chen, C.; Guo, W. Charge Carrier Separation Induced by Intrinsic Surface Strain in Pristine Zno Nanowires. *Appl. Phys. Lett.* **2010**, *97* (5), No. 053104.
(69) Tang, X.; Li, S.; Ma, Y.; Du, A.; Liao, T.; Gu, Y.; Kou, L. Distorted Janus Transition Metal Dichalcogenides: Stable Two-Dimensional Materials with Sizable Band Gap and Ultrahigh Carrier Mobility. *J. Phys. Chem. C* **2018**, *122* (33), 19153−19160.
(70) Bardeen, J.; Shockley, W. Deformation Potentials and Mobilities in Non-Polar Crystals. *Phys. Rev.* **1950**, *80* (1), 72−80.
(71) Qiao, J.; Kong, X.; Hu, Z.-X.; Yang, F.; Ji, W. High-Mobility Transport Anisotropy and Linear Dichroism in Few-Layer Black Phosphorus. *Nat. Commun.* **2014**, *5* (1), 4475.
(72) Cai, Y. Q.; Zhang, G.; Zhang, Y. W. Polarity-Reversed Robust Carrier Mobility in Monolayer Mos Nanoribbons. *J. Am. Chem. Soc.* **2014**, *136* (17), 6269−6275.
(73) Li, L.; Li, P.; Lu, N.; Dai, J.; Zeng, X. C. Simulation Evidence of Hexagonal-to-Tetragonal Znse Structure Transition: A Monolayer Material with a Wide-Range Tunable Direct Bandgap. *Adv. Sci.* **2015**, *2* (12), No. 1500290.
(74) Takagi, S.; Toriumi, A.; Iwase, M.; Tango, H. On the Universality of Inversion Layer Mobility in Si Mosfet's: Part I-Effects of Substrate Impurity Concentration. *IEEE Trans. Electron Devices* **1994**, *41* (12), 2357−2362.
(75) Zheng, M.; Li, Y.; Ding, K. N.; Zhang, Y. F.; Chen, W. K.; Lin, W. A Boron-Decorated Melon-Based Carbon Nitride as a Metal-Free Photocatalyst for N_2 Fixation: A Dft Study. *Phys. Chem. Chem. Phys.* **2020**, *22* (38), 21872−21880.
(76) Dimple; Jena, N.; Rawat, A.; De Sarkar, A. Strain and Ph Facilitated Artificial Photosynthesis in Monolayer Mos Nanosheets. *Journal of Materials Chemistry A* **2017**, *5* (42), 22265−22276.
(77) Li, F.; Shi, C.; Wang, D.; Cui, G.; Zhang, P.; Lv, L.; Chen, L. Improved Visible-Light Absorbance of Monolayer MoS_2 on Aln Substrate and Its Angle-Dependent Electronic Structures. *Phys. Chem. Chem. Phys.* **2018**, *20* (46), 29131−29141.
(78) Zhou, J.; Zhen, X. A Theoretical Perspective of the Enhanced Photocatalytic Properties Achieved by Forming Tetragonal ZnS/ZnSe Hetero-Bilayer. *Phys. Chem. Chem. Phys.* **2018**, *20* (15), 9950−9956.
(79) Wang, J.; Zhang, M.; Meng, J.; Li, Q.; Yang, J. Single- and Few-Layer Bioi as Promising Photocatalysts for Solar Water Splitting. *RSC Adv.* **2017**, *7* (39), 24446−24452.
(80) Ma, X.-Y.; Lewis, J. P.; Yan, Q.-B.; Su, G. Accelerated Discovery of Two-Dimensional Optoelectronic Octahedral Oxyhalides Via High-Throughput Ab Initio Calculations and Machine Learning. *J. Phys. Chem. Lett.* **2019**, *10* (21), 6734−6740.
(81) Ma, X.-Y.; Lyu, H.-Y.; Hao, K.-R.; Zhu, Z.-G.; Yan, Q.-B.; Su, G. High-Efficient Ab Initio Bayesian Active Learning Method and Applications in Prediction of Two-Dimensional Functional Materials. *Nanoscale* **2021**, *13* (35), 14694−14704.

https://doi.org/10.1021/acsomega.4c00803
ACS Omega 2024, 9, 32502−32512